Article

Developmental Cell

Iron-Dependent Callose Deposition Adjusts Root Meristem Maintenance to Phosphate Availability

Graphical Abstract

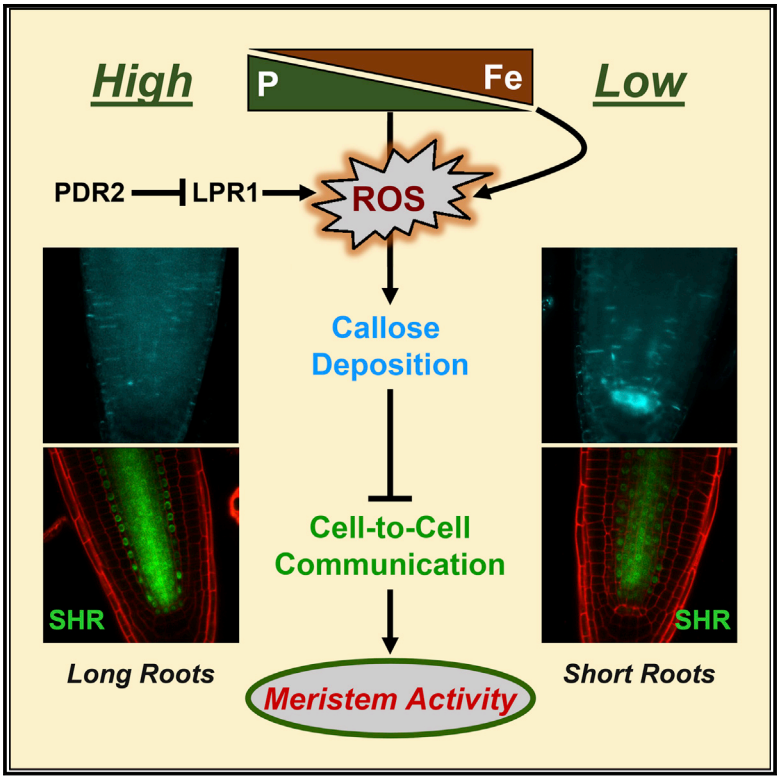

Authors

Jens Müller, Theresa Toev, ..., Katharina Bürstenbinder, Steffen Abel

Correspondence

sabel@ipb-halle.de

In Brief

Edaphic (soil-derived) cues inform root development. Müller et al. show that antagonistic interactions between phosphate and iron availabilities adjust root growth via meristem-specific callose deposition, which regulates cell-to-cell communication in the stem cell niche. LPR1 ferroxidase-dependent redox signaling, initiated in the root apoplast, is central to local phosphate sensing.

Highlights

- Primary root growth inhibition under low-phosphate conditions needs iron availability
- Phosphate limitation triggers apoplastic iron and callose deposition in root meristems
- Callose deposition inhibits symplastic communication in the root stem cell niche
- Root meristem-specific *LOW PHOSPHATE ROOT1* encodes a cell-wall-targeted ferroxidase

Müller et al., 2015, Developmental Cell *33*, 216–230
April 20, 2015
http://dx.doi.org/10.1016/j.devcel.2015.02.007

CellPress

CellPress

Developmental Cell
Article

Iron-Dependent Callose Deposition Adjusts Root Meristem Maintenance to Phosphate Availability

Jens Müller,[1] Theresa Toev,[1] Marcus Heisters,[1] Janine Teller,[1] Katie L. Moore,[2] Gerd Hause,[3] Dhurvas Chandrasekaran Dinesh,[1] Katharina Bürstenbinder,[1] and Steffen Abel[1,4,5,*]
[1]Department of Molecular Signal Processing, Leibniz Institute of Plant Biochemistry, 06120 Halle (Saale), Germany
[2]Department of Materials, University of Oxford, Oxford OX1 3PH, UK
[3]Biocenter, Martin Luther University Halle-Wittenberg, 06120 Halle (Saale), Germany
[4]Institute of Biochemistry and Biotechnology, Martin Luther University Halle-Wittenberg, 06120 Halle (Saale), Germany
[5]Department of Plant Sciences, University of California, Davis, Davis, CA 95616, USA
*Correspondence: sabel@ipb-halle.de
http://dx.doi.org/10.1016/j.devcel.2015.02.007

SUMMARY

Plant root development is informed by numerous edaphic cues. Phosphate (Pi) availability impacts the root system architecture by adjusting meristem activity. However, the sensory mechanisms monitoring external Pi status are elusive. Two functionally interacting *Arabidopsis* genes, *LPR1* (ferroxidase) and *PDR2* (P5-type ATPase), are key players in root Pi sensing, which is modified by iron (Fe) availability. We show that the *LPR1-PDR2* module facilitates, upon Pi limitation, cell-specific apoplastic Fe and callose deposition in the meristem and elongation zone of primary roots. Expression of cell-wall-targeted LPR1 determines the sites of Fe accumulation as well as callose production, which interferes with symplastic communication in the stem cell niche, as demonstrated by impaired SHORT-ROOT movement. Antagonistic interactions of Pi and Fe availability control primary root growth via meristem-specific callose formation, likely triggered by LPR1-dependent redox signaling. Our results link callose-regulated cell-to-cell signaling in root meristems to the perception of an abiotic cue.

INTRODUCTION

Vigorous development of the seed radicle into an elaborate root system is critical for plant survival and performance because roots provide an extensive interface for water uptake, mineral nutrition, and chemical interactions with the rhizosphere. Root development, which is highly plastic and responsive to numerous edaphic cues, has been studied extensively in *Arabidopsis thaliana* (Petricka et al., 2012). The simple anatomy of its root, comprising the vascular cylinder and three radial cell layers (endodermis, cortex, and epidermis), is maintained by the stem cell niche (SCN) of the root apical meristem (RAM). The SCN is patterned during embryogenesis and includes the quiescent center (QC) and contacting pluripotent cells. These initials are perpetual sources of daughter cells that generate the lineages of transit-amplifying (TA) cells of the proximal meristem (Dolan et al., 1993; Scheres, 2007). At the boundary to the elongation zone (transition zone), TA cells exit the cell cycle, expand, and differentiate by acquiring tissue-specific characteristics (Perilli et al., 2012). The position of the transition zone determines RAM size and is directly related to the root growth rate (Baum et al., 2002).

Cell-to-cell signaling is a key organizing principle in metazoan development. RAM and SCN maintenance require the precise coordination of cell division and differentiation, which depends on the directional intercellular transport of mobile signals (Gallagher et al., 2014; Perilli et al., 2012). For example, the QC maintains adjacent stem cells via unknown short-range signals that prevent their differentiation (Scheres, 2007; van den Berg et al., 1997). The transcription factor SHORT-ROOT (SHR) moves from the stele into the QC and endodermis to determine cell fate, partly by interaction with SCARECROW (Cui et al., 2007; Nakajima et al., 2001; Sabatini et al., 2003). Two major routes of cell-to-cell communication are known in plants. Intercellular translocation of cargo is facilitated by exo- and endocytosis (Contento and Bassham, 2012) or by direct symplastic transport via specialized channels, called plasmodesmata (PD) (Burch-Smith and Zambryski, 2012). Metabolites, small proteins, and RNAs may transverse PD by diffusion, whereas other macromolecules interact with PD and move by a targeted mechanism. Symplastic trafficking can be tuned by modification of PD structure or deposition of callose (a β-1,3 glucan) at the PD neck region (Benitez-Alfonso et al., 2013; Zavaliev et al., 2011). During numerous developmental processes or environmental responses, callose production controls PD conductivity, which is counteracted by specific PD-localized β-1,3 glucanases (Burch-Smith and Zambryski, 2012). There is growing evidence that reactive oxygen species (ROS) and redox signaling regulate callose deposition and symplastic permeability (Benitez-Alfonso et al., 2011; Stonebloom et al., 2009). In root development, PD and, possibly, callose turnover are essential for SHR movement (Vatén et al., 2011) or for determining the pattern of lateral root formation (Benitez-Alfonso et al., 2013). However, the mechanisms that connect callose-regulated cell-to-cell signaling in the RAM to the perception of soil-borne cues are elusive.

The mineral nutrient inorganic phosphate (Pi) constitutes a major nexus in metabolism, and its availability directly impacts vital plant functions. Pi immobility and resultant Pi limitation are pervasive in soils and caused by complex chemistries involving Fe and other metals. To cope with Pi shortage, plants attenuate primary root extension, promote lateral root development, and stimulate root hair formation, plastic growth responses thought to maximize Pi interception in topsoil (Abel, 2011; Péret et al., 2011). Studies in *Arabidopsis* identified mutants and accessions with altered Pi sensitivities of primary root growth and showed that external Pi is monitored by the root apex to locally inform root development (Reymond et al., 2006; Svistoonoff et al., 2007; Ticconi et al., 2004, 2009). Recent work uncovered a central role of *LPR1* (*LOW PHOSPHATE ROOT1*), its close paralog *LPR2*, and *PDR2* (*PHOSPHATE DEFICIENCY RESPONSE2*) in local Pi sensing. *PDR2* was isolated by mutagenesis of accession Col (Ticconi et al., 2009), and *LPR1* was identified in recombinant inbred lines of accessions, Bay and Sha, which show opposite root growth responses to low Pi (Svistoonoff et al., 2007). *LPR1* and *PDR2* encode proteins of the secretory pathway (a multicopper oxidase and the single P5-type ATPase, respectively), and their expression domains overlap in the distal RAM. The *LPR* genes and *PDR2* interact genetically (the insensitive *lpr1lpr2* mutations suppress the hypersensitive *pdr2* short root phenotype in low Pi) and are required for SCN and RAM maintenance in Pi-deprived roots (Svistoonoff et al., 2007; Ticconi et al., 2009). Intriguingly, external Fe availability modifies the Pi-dependent root growth response (Svistoonoff et al., 2007; Ticconi et al., 2009; Ward et al., 2008). Here we show that the *LPR1-PDR2* module mediates cell-specific Fe deposition in cell walls of the RAM and elongation zone during Pi limitation. Fe accumulation coincides with sites of callose deposition, which interferes with cell-to-cell communication and SCN maintenance, as revealed by impaired SHR movement. We provide evidence for apoplastic LPR1 ferroxidase activity and propose that antagonistic interactions of Pi and Fe availability adjust the primary root growth rate via RAM-specific callose deposition, likely triggered by LPR1-dependent redox signaling.

RESULTS

Root Growth Inhibition in Low Pi Depends on External Fe

Because Fe availability modifies root growth in low Pi (Svistoonoff et al., 2007; Ward et al., 2008), we studied in detail the interactions of both nutrients during primary root development. We used a set of six *A. thaliana* accessions (Col, Bay, and Sha) and Col mutant lines (*pdr2*, *lpr1lpr2*, and *lpr1lpr2pdr2*) that display similar root growth rates on +Pi but contrasting sensitivities of growth inhibition on –Pi medium (Svistoonoff et al., 2007; Ticconi et al., 2009). Compared with Col and Sha, *pdr2* roots responded in a hypersensitive fashion to –Pi, whereas roots of Bay, *lpr1lpr2*, and *lpr1lpr2pdr2* were insensitive, with the triple mutant showing a genetic interaction of the *LPR* and *PDR2* genes. Interestingly, inhibition of root growth was rescued by Fe omission (–Pi–Fe), approaching the growth observed in +Pi (Figure 1A).

Root extension and RAM size are controlled by the rates of cell division and differentiation as well as by the number and length of elongating cells (Beemster and Baskin, 1998). We measured, in nutrient shift studies, the number of meristematic and elongating cells and the length of the first differentiated cell in a single trichoblast file. After transfer to +Pi, the three parameters did not change considerably between genotypes for up to 40 hr (Figure 1B). However, within 20 hr on –Pi, roots of *pdr2* showed a significant decrease in the number of meristematic cells that sharply dropped to ~25% after 40 hr, suggesting a shift from cell division to differentiation. For the Col and Sha accessions, a significant decline was observed after 40 hr, whereas no reduction was detectable for the three insensitive lines. On the other hand, the number of elongating cells and the length of the first root hair-forming cell were reduced strongly in roots of the sensitive lines within 20 hr on –Pi, pointing to early differentiation of elongating cells. Both parameters did not change for *lpr1lpr2* and *lpr1lpr2pdr2* roots. The Bay accession showed only a slight reduction in trichoblast length. Importantly, transfer to –Pi–Fe medium prevented RAM reduction and early cell differentiation for all genotypes (Figure 1B). Therefore, Pi deficiency-induced root growth inhibition depends on external Fe presence and is initiated by accelerated differentiation of elongating cells, followed by a decline in meristematic cells.

Pi Limitation Stimulates Cell-Specific Fe Accumulation in Root Tips

Several studies reported Fe overload in Pi-deprived plants (Abel, 2011). To visualize Pi-dependent Fe distribution in roots, we used a sensitized, Fe-specific histochemical procedure (Perls/diaminobenzidine [DAB] staining) that reports labile (non-heme) Fe^{3+} and some Fe^{2+} (Meguro et al., 2007; Roschzttardtz et al., 2009). For Pi-replete seedlings, we detected Fe only in the root apex, a pattern that changed dramatically within 20 hr after transfer to –Pi (Figure 1C; Figure S1A). Although Col, *pdr2*, and Sha roots revealed Fe accumulation along the entire root axis, including the RAM, the three insensitive lines showed increased Fe staining only in the mature root region, suggesting that differential Fe distribution in root tips, and not general Fe overload, determines the Pi growth response. Direct measurement of Fe content in whole roots revealed Fe hyperaccumulation in *pdr2* on –Pi but similar Fe levels in Col and *lpr1lpr2* roots (Figure S1B). To estimate the relative contribution of Fe^{3+} and Fe^{2+} to the labile Fe pool, we compared Perls/DAB and Turnbull/DAB staining of root tips because the latter method is specific for Fe^{2+} (Meguro et al., 2007). The data revealed much weaker Fe^{2+} than Fe^{3+} staining irrespective of Pi supply and genotype (Figure S1C). Therefore, the dynamics of histological Fe detection are largely caused by changes in labile Fe^{3+} pools.

Previous work implicated the root apex in external Pi sensing (Svistoonoff et al., 2007). We examined cell-type-specific Fe distribution in Pi-replete root tips and detected Fe mainly in the root cap (RC) and SCN, with stronger Fe staining in the RC of Col, *pdr2*, and Sha roots (Figure 1C). Within 20 hr after transfer to –Pi, Col and Sha showed Fe accumulation in the rapidly differentiating elongation zone, whereas *pdr2* revealed Fe hyperaccumulation in the entire root tip. Such a distribution was not observed for the three insensitive lines, which showed diminished Fe staining during continued exposure to –Pi (Figure 1C). Perls/DAB staining was not detectable after transfer to –Pi–Fe medium, which corroborates the Fe specificity of the method and suggests that the elevated Fe content of Pi-deprived roots depends on external Fe availability (Figure S1A). We used the

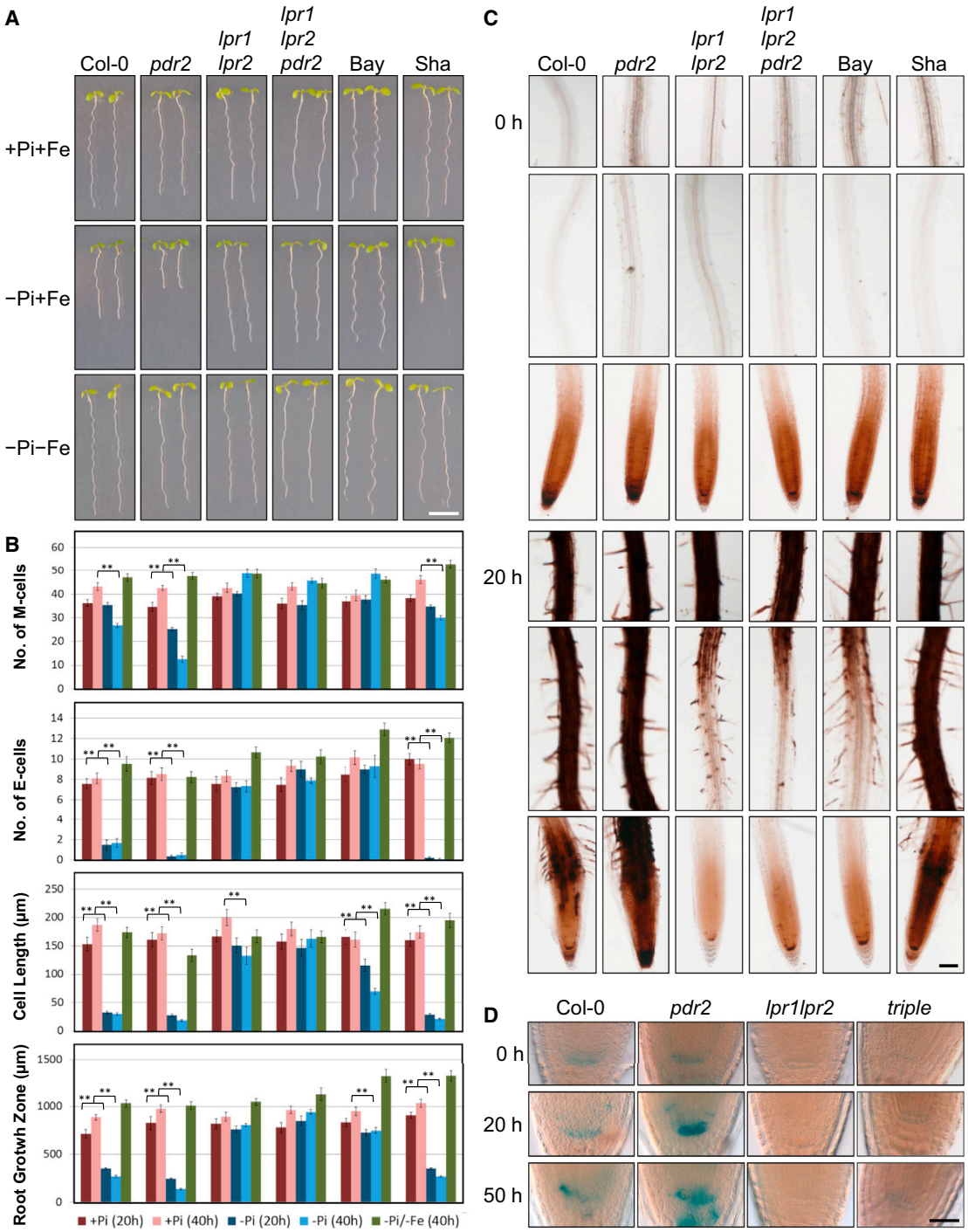

Figure 1. Fe-Dependent Root Growth Inhibition in Low Pi

(A) Seeds were germinated on +Pi agar (4 days) and transferred to +Pi, –Pi, or –Pi medium without Fe (–Pi–Fe). Representative images were taken 3 days after transfer. Scale bar, 1 cm.

(B) Root growth analysis. Top graphs (order of genotypes as in A): number of meristematic (M-cells) and elongating cells (E-cells). Bottom graphs: size of the first differentiated cell and root growth zone (meristem plus elongation zone). Shown are the means of three independent experiments (±SE, n = 12–18, **p < 0.001, Student's t test).

(C) Fe accumulation and distribution in primary roots. Seeds were germinated on +Pi (4 days) and transferred to –Pi for 20 hr prior to Perls/DAB staining. The top panels of each time point show the mature root zone. The center and bottom panels depict the early differentiation zone and root apical region, respectively. Scale bar, 100 µm.

(D) Fe staining (Perls only) of the root SCN (transfer as above). Scale bar, 25 µm. triple, *lpr1lpr2pdr2*.

See also Figure S1.

less sensitive Perls method (no DAB enhancement) to monitor Fe distribution in the SCN and detected Fe largely in the QC of Pi-replete Col and *pdr2* roots (Figure 1D). Fe deposition in the SCN increased within 20 hr after transfer to –Pi and was notably stronger for *pdr2*. Root tips of *lpr1lpr2* never appreciably stained for Fe (Figure S1D), and the *lpr1lpr2pdr2* mutant showed only faint staining after transfer to –Pi, which supports *lpr1lpr2* epistasis to *pdr2* (Figure 1D).

Cell-Specific Fe Deposition in the Root Apoplast

We further studied Fe distribution on sections of Perls/DAB-stained Col and *pdr2* root tips. In addition to the RC and SCN of Pi-replete roots, Fe was commonly detected in the cortex of the root apex (Figures 2A and 2F). Within 20 hr on –Pi, staining of Col roots indicated local Fe accumulation within the apoplast surrounding SCN cells and cortical cells of the shortened elongation zone (Figures 2B–2D). In *pdr2*, elevated apoplastic Fe was detected mainly in the SCN and distal root meristem (Figures 2G–2I). Both lines also accumulated Fe in the differentiation zone, where it was deposited as a plaque at the outgrowing tip of root hairs (Figures 2E and 2J). High-resolution images of counterstained, plasmolyzed root cells clearly showed cell-wall-associated Perls/DAB staining (Figures 2K and 2L). Sections of *lpr1lpr2* and *lpr1lpr2pdr2* root tips revealed diminished local Fe deposition in the SCN or cortex under –Pi condition (Figure S2).

We confirmed apoplastic Fe localization by high-resolution secondary ion mass spectrometry (NanoSIMS) elemental mapping (Moore et al., 2011) of semi-thin sections prepared from *pdr2* roots. The images revealed apoplastic co-localization of ^{56}Fe- and ^{31}P-derived ions in the SCN of Pi-replete roots (Figures 2M–2R). After transfer to –Pi, ^{56}Fe signals, but no ^{31}P ions, were recorded for the apoplast (Figures 2S–2V), which showed signs of expansion, as suggested by gaps between SCN cells (Figure 2S). The data confirm cell-specific Fe accumulation in Pi-deprived root meristems and indicate dynamic colocalization of both ions in the apoplast, depending on external Pi availability.

Pi-Dependent Callose Deposition Inhibits Symplastic Communication

Because NanoSIMS imaging indicated apoplast expansion in –Pi, we prepared root sections for ultrastructural analysis. Indeed, on –Pi (20 hr), Col and *pdr2* root meristems accumulate electron-translucent cell wall material that is largely restricted to the SCN (Figure 3A; Figure S3A). High-resolution images revealed accumulation of secretory vesicles and extreme thickening of QC cell walls in *pdr2*, which is less pronounced in Col and not evident in *lpr1lpr2* roots (Figure 3A, bottom). However, Col roots revealed substantial cell wall thickening within the cortex file of the elongation zone, particularly at sites of Fe accumulation (Figure 3D). Propidium iodide (PI) staining indicated frequent events of cell death only in the *pdr2* QC (Figure S3B), which is likely a consequence of massive cell wall deposition and may explain accelerated RAM differentiation.

Because the irregular pattern of extra cell wall material is indicative of callose deposition, we examined Pi-dependent callose formation by immunogold labeling and aniline blue staining (Figures 3B and 3C). Within 20 hr on –Pi, Col roots revealed callose deposition in the SCN and cortex cells of the elongation zone, a pattern strikingly similar to that of Fe accumulation (Figure 3D). In *pdr2* roots, massive callose formation occurred predominantly in the SCN and RAM, whereas no extra callose deposition was observed for the three insensitive genotypes. Enhanced callose formation was not observed on −Pi−Fe, indicating that callose production in –Pi depends on Fe availability (Figure S3C).

Because callose deposition may affect PD permeability, we used two GFP reporter lines to study Pi-dependent regulation of symplastic transport (Figure 4). GFP expressed under control of the companion cell-specific gene promoter *SUCROSE-H$^+$ SYMPORTER 2* (*pSUC2*) passively diffuses through PD from the phloem into surrounding tissues (Benitez-Alfonso et al., 2009; Imlau et al., 1999). Within 2 days on –Pi, GFP movement into primary root tips was inhibited greatly in wild-type (Col) plants expressing *pSUC2::GFP*. As expected, GFP diffusion was impaired severely in *pdr2* but unaffected in *lpr1lpr2* roots (Figure 4A). SHR is a key regulator of radial root patterning and acts in a concentration-dependent manner (Helariutta et al., 2000; Koizumi et al., 2012; Wu et al., 2014). We examined *pSHR::SHR∼GFP* expression in the RAM of the wild-type (Col), *pdr2*, and *lpr1lpr2* upon transfer to –Pi. Again, SHR∼GFP movement was impaired severely in *pdr2* but unaltered in *lpr1lpr2* root meristems (Figure 4B). Analysis of wild-type roots indicated reduced SHR∼GFP fluorescence in the QC within 12 hr, which declined to intensities below the detection limit after 48 hr (Figures 4C and 4D). We further noticed the formation of a premature middle cortex layer (Figure 4C), which is likely caused by restricted SHR movement into the endodermis (Koizumi et al., 2012; Paquette and Benfey, 2005). Therefore, SCN-specific callose deposition in –Pi modulates RAM maintenance, likely via symplastic cell-to-cell communication.

LPR1 Expression Triggers Fe Accumulation and Callose Deposition in Low Pi

The similar patterns of LPR1-dependent Fe and callose accumulation in –Pi prompted us to determine the *LPR1* expression domain and consequences of *LPR1* overexpression. Analysis of transgenic *pLPR1^{Col}::GUS* roots (Col) revealed the highest *LPR1* promoter activity within the SCN and weaker β-glucoronidase (GUS) expression in endodermal cell layers and provascular tissues, which only slightly expanded into the maturation zone upon Pi deprivation (Figure 5A). Steady-state *LPR1* mRNA levels did not appreciably respond to –Pi and were similar for wild-type and *pdr2* roots (data not shown). Notably, cell-specific *pLPR1::GUS* expression correlated with patterns of Fe and callose deposition in Pi-starved wild-type (Col) root tips (Figures 1C and 3C).

We generated transgenic *CaMV p35S::LPR1* and *p35S::SP^{LPR1}∼GFP∼LPR1* plants (Col) for analysis of root phenotypes (Figure 5; Figure S4). Several *p35S::LPR1* lines expressing elevated levels of *LPR1* mRNA and LPR1 protein showed development of a truncated root system only after germination on –Pi, which was similar to the *pdr2* root phenotype. The root tips stained intensely for Fe and callose on –Pi only, demonstrating a critical role of LPR1 for Fe accumulation, callose deposition, and root growth inhibition in response to –Pi (Figure 5B; Figures S4A–S4E). *p35S::SP^{LPR1}∼GFP∼LPR1* lines showed partial transgene silencing in the RAM but stronger GFP∼LPR1 expression in the RC (Figure 5C). For all *LPR1*-overexpressing lines, nutrient shift studies revealed Fe and callose accumulation in

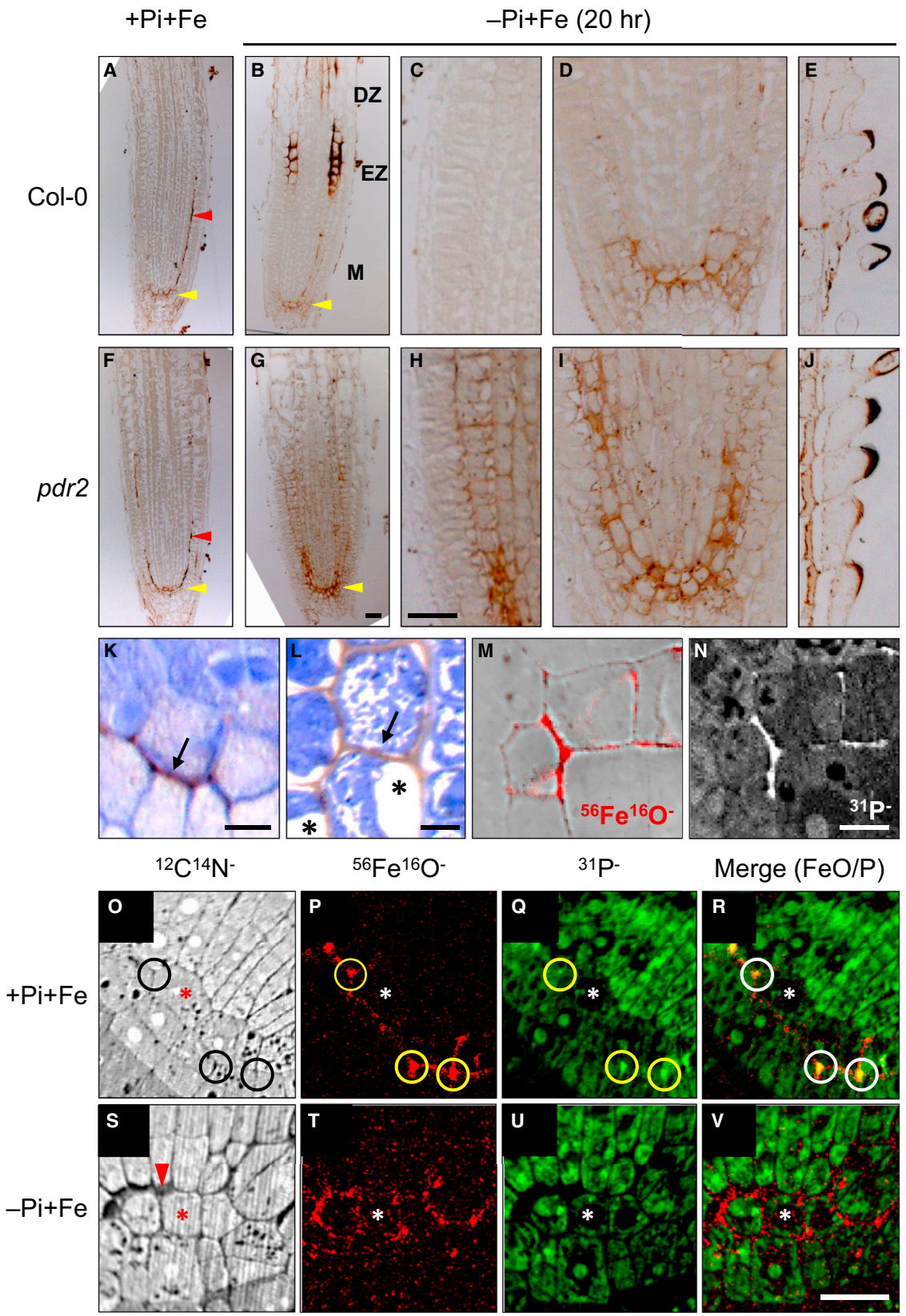

(legend on next page)

the RC on –Pi only, indicating that *LPR1* expression determines the sites of Fe accumulation and callose deposition (Figure 5D).

LPR1 Encodes a Cell Wall Ferroxidase

LPR1 and *LPR2* code for multicopper oxidases (MCOs) of unknown substrate specificity (Svistoonoff et al., 2007). Polyphenol oxidases (laccases) and proteins related to ferroxidases are the largest group in the MCO family across all phyla (Hoegger et al., 2006). Yeast Fet3p is the best characterized ferroxidase, which couples the oxidation of four Fe^{2+} ions to the reduction of O_2 to $2H_2O$ via four catalytic Cu sites organized in two centers, the mononuclear Cu site (T1) and the trinuclear Cu cluster (T2/T3). Structure-function studies identified three amino acid residues near the T1 site (E185, D283, and D409) that are critical for Fe^{2+} binding and electron transfer (Stoj et al., 2006). Alignment of LPR and Fetp sequences showed conservation of the Cys and ten His residues coordinating the four Cu sites but failed to identify acidic residues in LPR proteins that may complex Fe^{2+} (Figure S5A). Homology modeling of LPR1 and LPR2 and structural superimposition with the crystal structure of Fet3p (Figures 5E and 5F; Figure S5B) indicated the presence of a spatially conserved acidic triad in LPR1 (E269, D370, and D462) and LPR2 (E271, D372, and D464), which prompted us to test ferroxidase activity.

Using a ferrozine-based assay, we compared ferroxidase activity in root extracts of wild-type (Col) and *p35S::LPR1* plants and measured up to 5-fold higher specific activities for the LPR1 overexpression lines. Ferroxidase activity correlated approximately with steady-state *LPR1* mRNA and protein levels (Figures S4F–S4H). We confirmed this observation by transient expression of $p35S::SP^{LPR1}{\sim}GFP{\sim}LPR1$ in tobacco leaves, which demonstrated LPR1-dependent expression of ferroxidase activity in planta (Figure 5G). We previously detected LPR1 in the ER (Ticconi et al., 2009). Because ferroxidases typically reside in the extracellular matrix, we reexamined $SP^{LPR1}{\sim}$GFP$\sim$LPR1 targeting in transgenic *Arabidopsis* roots. In addition to ER localization, our data revealed cell-wall-derived GFP$\sim$LPR1 fluorescence (Figure 5H). LPR1 cell wall targeting was confirmed in transgenic $pUBQ10::SP^{LPR1}{\sim}GFP{\sim}LPR1$ plants, which showed considerably lower GFP$\sim$LPR1 expression (Figure 5I; Figure S5C), and in cell wall extracts after sequential washing of suspension-cultured wild-type (Col) cells (Figure 5J). Therefore, LPR1 ferroxidase functions in the apoplast.

LPR1-Dependent Fe Accumulation in Low Pi Correlates with ROS Production

Recent studies have implicated ROS and cellular redox status in the regulation of symplastic transport, which is controlled by callose turnover at the PD neck region (Benitez-Alfonso et al., 2011; Stonebloom et al., 2009; Zavaliev et al., 2011). Accumulation of apoplastic labile Fe^{3+} in root tips is a potential source of catalytic Fe, which participates in ROS generation and Fe redox cycling (Kosman, 2010; Meguro et al., 2007). The similar pattern of apoplastic Fe^{3+} and callose accumulation in root meristems on –Pi prompted us to monitor LPR1-dependent ROS formation. We observed apoplastic ROS (carboxylated 2′,7′-dichlorodihydrofluorescein diacetate [C-H2DCFDA] staining) and superoxide (Nitro blue tetrazolium [NBT] staining) formation in root tips of the sensitive but not insensitive lines within 12–24 hr after transfer from +Pi to –Pi medium (Figure 6). Furthermore, overexpression of $p35S::SP^{LPR1}{\sim}GFP{\sim}LPR1$ enhanced ROS production in the RC on –Pi only (Figure 5D), which suggests that LPR1-dependent Fe oxidation generates ROS in low Pi.

High Pi Availability Counters Fe Excess

The striking correlation of Fe accumulation, ROS production, and callose deposition in Pi-starved root tips raised the question whether excess Fe and its presumed toxicity triggers root growth inhibition, as proposed previously (Ward et al., 2008). We therefore transferred seedlings from control agar to +Pi medium supplemented with 10-fold higher (500 μM) Fe (+Pi++Fe). When compared with transfer to –Pi+Fe, we noticed Fe hyperaccumulation in Col root meristems, which was augmented further in *pdr2*. No Fe staining in *lpr1lpr2* root meristems and only faint staining in *lpr1lpr2pdr2* was detectable (Figure 7A). Measurement of Fe in whole roots confirmed Fe overaccumulation in +Pi++Fe medium, which was similar for all genotypes (Figure S1B). Surprisingly, Fe overload did not elicit superoxide formation and callose deposition. Likewise, RAM organization was maintained, and root growth was significantly less inhibited compared with plants on –Pi (Figure 7B). Therefore, LPR1-controlled Fe accumulation and callose deposition in root tips likely depends on extracellular Pi:Fe ratios.

Root Apical Fe Sequestration Mediates the Growth Response to Low Pi

Because the growth response to –Pi requires external Fe and the *LPR1* expression domain delimits Fe accumulation and callose formation, we monitored Fe acquisition by root tips. IRON-REGULATED TRANSPORTER 1 (IRT1), located in the plasma membrane of differentiated root epidermal cells, constitutes the major feedback-regulated Fe uptake system in *Arabidopsis* (Kobayashi and Nishizawa, 2012; Vert et al., 2002). Irrespective of Pi supply, wild-type (Col) and *irt1-1* knockout plants showed

Figure 2. Cell-Specific Fe Deposition in the Root Apoplast

(A–J) Semi-thin (1-μm) longitudinal sections of Perls/DAB-stained root tips of Col (A–E) and *pdr2* (F–J) seedlings after transfer from +Pi to –Pi medium (20 hr). (C and D) and (H and I) show magnifications of the RAM in (B) and (G), respectively. (E) and (J) show root hair bulges. Yellow and red arrowheads point to the QC and cortex cell layer, respectively. M, meristem; EZ, elongation zone; DZ, differentiation zone. Scale bar, 25 μm.

(K and L) Toluidine blue counterstain of Col root stem cells (K) and cortex cells (L) after transfer to –Pi. Arrows point to apoplastic Perls/DAB staining, and asterisks mark plasmolyzed protoplasts. Scale bar, 5 μm.

(M–V) NanoSIMS images of semi-thin (1-μm) longitudinal sections of *pdr2* root tips 20 hr after transfer. Shown are high-magnification images of stem cells showing apoplastic ^{56}Fe (M) and ^{31}P (N) signals after transfer to +Pi medium. Scale bar, 5 μm. Also shown are overview images after transfer to +Pi (O–R) or –Pi (S–V). Circled are Fe- and P-containing extracellular deposits (O–R). The arrowhead points to local cell wall expansion, and asterisks mark the QC. Scale bar, 10 μm.

See also Figure S2.

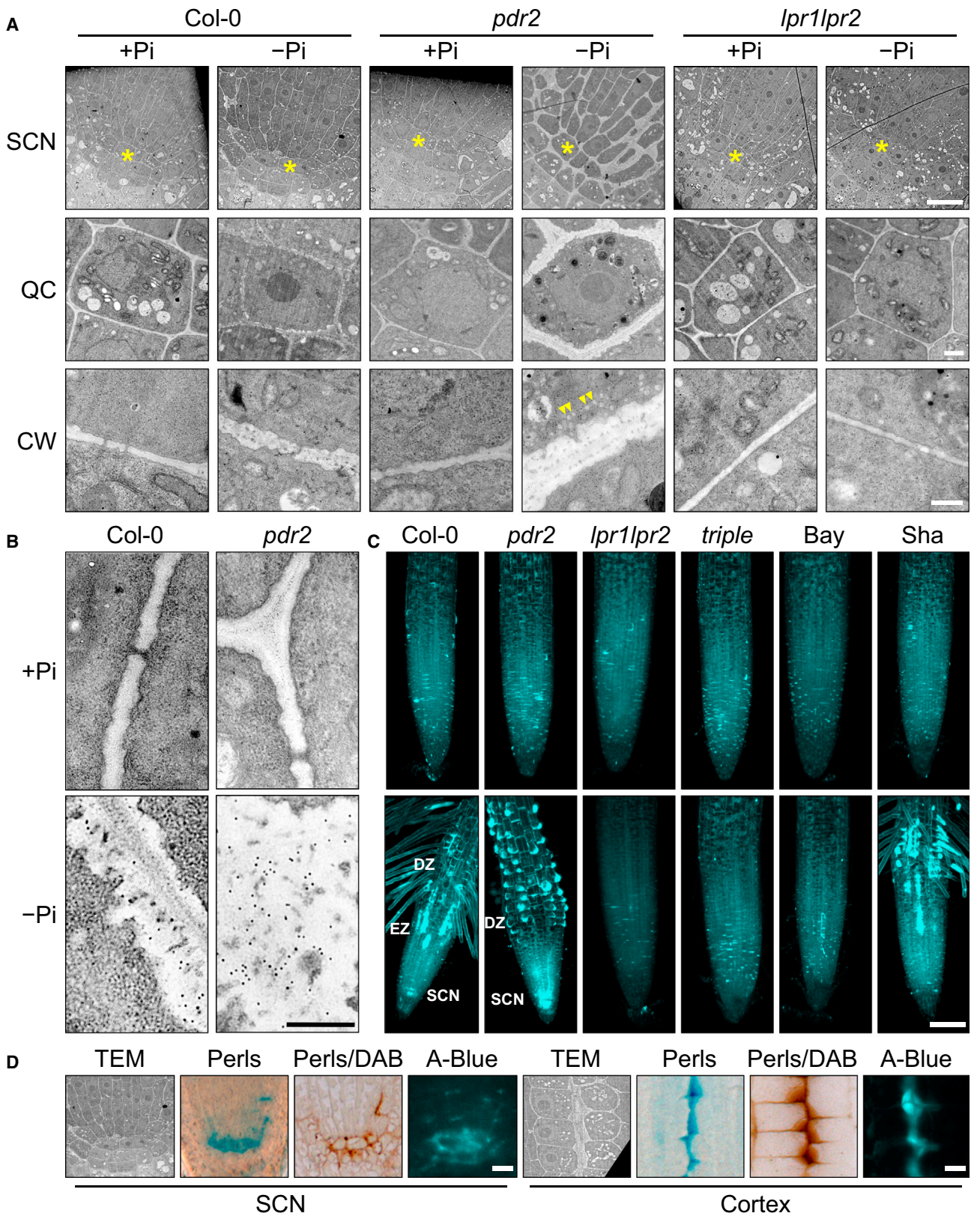

(legend on next page)

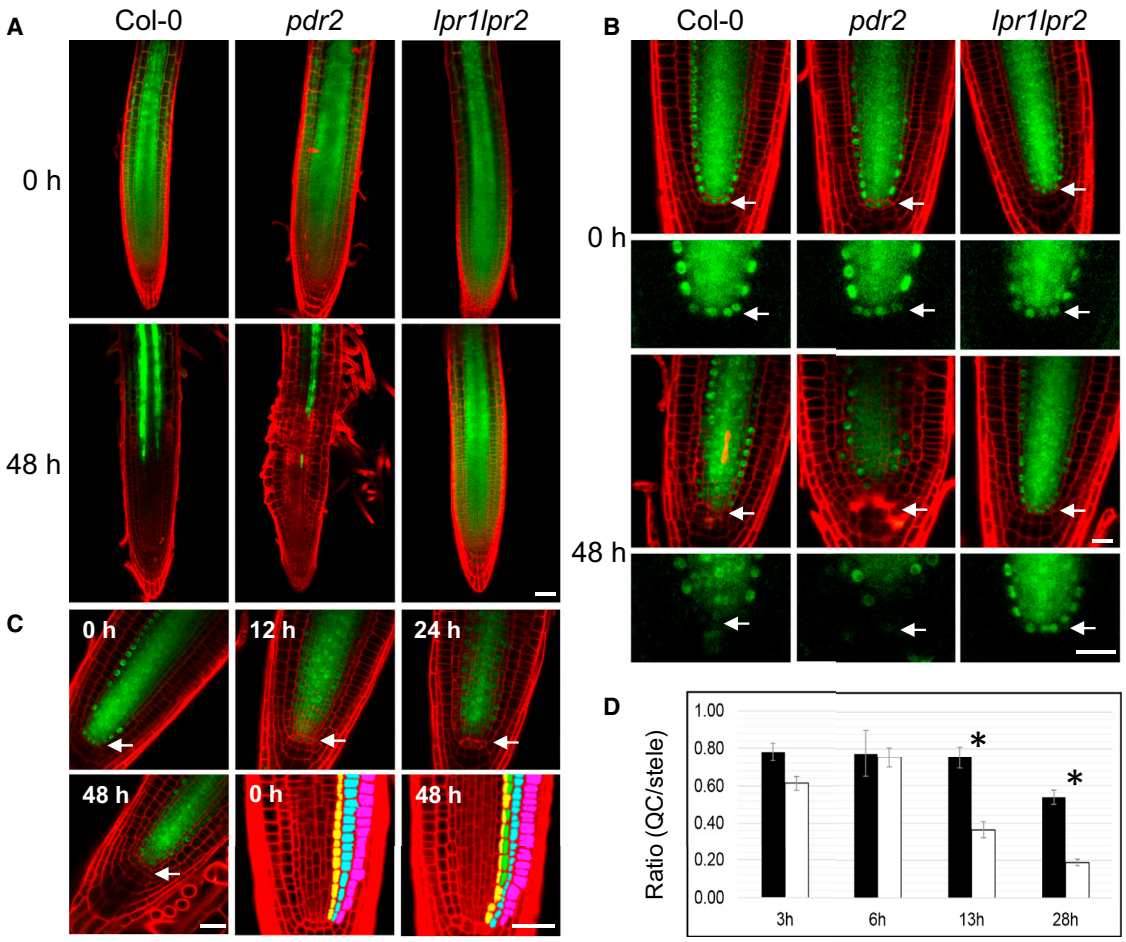

Figure 4. Pi-Dependent Inhibition of Symplastic Trafficking in the RAM

Transgenic wild-type (Col) seeds were germinated for 4 days prior to transfer to +Pi or −Pi medium. Primary roots were counterstained with PI (red fluorescence) and analyzed for GFP fluorescence (green).

(A) *pSUC2::GFP* expression 2 days after transfer. Scale bar, 100 μm.

(B) *pSHR::SHR∼GFP* expression 2 days after transfer. Arrows point to the QC. Scale bar, 50 μm.

(C) Time course of *pSHR::SHR∼GFP* expression in the wild-type (Col) after transfer to –Pi. The bottom right panels indicate the formation of a middle cortex layer 48 hr after transfer (as found in 89% of primary root meristems examined; n = 28). Cell layers are false-color coded (middle cortex cells in green). Scale bar, 50 μm.

(D) Quantitative analysis of SHR∼GFP movement in the wild-type (Col) from the stele into the QC after transfer to +Pi (black bars) or –Pi (white bars). The QC-to-stele fluorescence ratios (±SE, n = 16–26 cells/time point, $p < 0.001$, Student's t test) were calculated using ImageJ.

comparable primary root growth (Figure 7C) and Fe staining in root meristems (Figure S6). This suggests an IRT1-independent Fe uptake system restricted to the root tip. To test this prediction, we transferred Col, *pdr2*, and *lpr1lpr2* seedlings to either +Pi or –Pi and cut off the primary root tips at the proximal meristem border. The detached root tips continued to grow on the agar surface and showed, within 1 day, the genotype-specific growth response to Pi availability and characteristic Fe staining pattern (Figure 7D). Therefore, root tip-specific, LPR1-dependent Fe acquisition, and not long-distance Fe import from mature tissues, mediates the developmental response of root meristems to Pi availability.

Figure 3. Pi-Dependent Callose Deposition in the Root Apex

(A) Electron micrographs of ultra-thin (90-nm) longitudinal sections of the SCN and ultrastructural analysis of QC cells and cell walls after transfer of 4-day-old plants to +Pi or −Pi medium (20 hr). Asterisks label QC cells in the overview row (SCN). The rows labeled QC and CW show high-resolution images of QC cells and cell walls, respectively. Arrowheads point to secretory vesicles. Scale bars, 10 μm (SCN), 1 μm (QC), and 0.5 μm (CW).

(B) Callose detection by immunogold labeling in Col and *pdr2* roots. Labeling is detected only in the cell walls of Pi-deprived roots. Scale bar, 0.5 μm.

(C) Aniline blue staining (3D projections) of primary roots after transfer of 4-day-old plants to +Pi or −Pi medium (2 days). Scale bar, 100 μm. triple, *lpr1lpr2pdr2*.

(D) Comparison of transmission electron micrographs (TEM), Fe staining (Perls or Perls/DAB), and callose staining by aniline blue (A-Blue) in the primary root apex of a Col seedling after transfer from +Pi+Fe to −Pi+Fe medium. Shown are typical regions of Fe accumulation and callose deposition within the SCN and cortex of the shortened transition/elongation zone. Scale bars, 10 μm.

See also Figure S3.

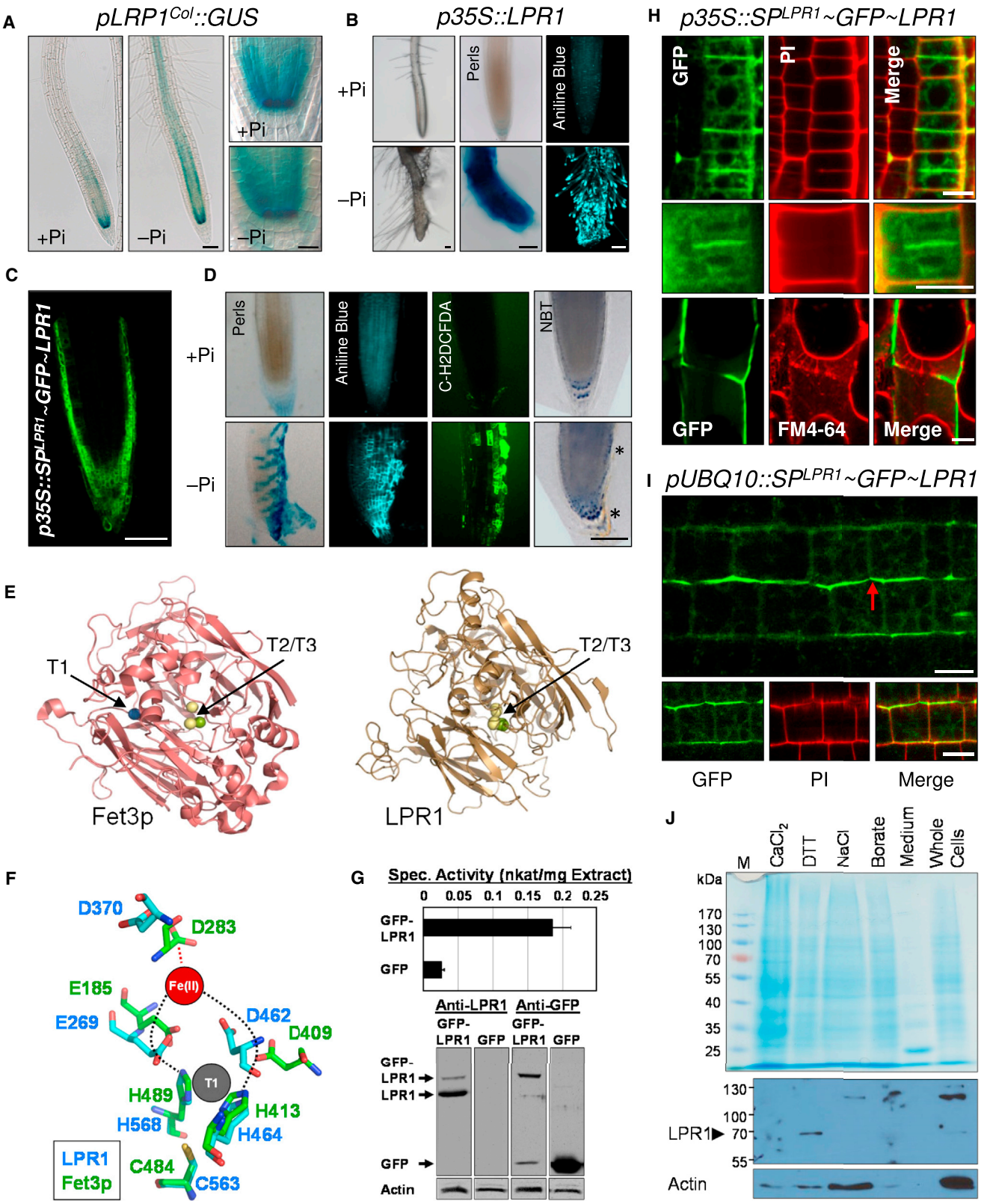

Figure 5. Properties of LPR1 and Consequences of LPR1 Overexpression

(A) Expression of *pLPR1::GUS* after transfer of 4-day-old plants to +Pi or −Pi medium (24 hr). Shown are primary roots (left; scale bar, 100 μm) and the SCN (right; scale bar, 20 μm).

(legend continued on next page)

DISCUSSION

Sessile plants employ indeterminate growth strategies for habitat exploration or stress evasion. Post-embryonic development is therefore profoundly responsive to environmental cues. We provide significant insights into the molecular processes that adjust root development to Pi availability. Pi is the predominant nutritional factor controlling primary root length (Kellermeier et al., 2014), presumably to favor topsoil foraging of the immobile nutrient. External Pi status is sensed locally at the root apex, and an inadequate Pi supply attenuates primary root growth via early inhibition of cell elongation followed by meristem size reduction (Sánchez-Calderón et al., 2005; Svistoonoff et al., 2007; Ticconi et al., 2004). Our study uncovers an essential role for Fe in root Pi sensing and reveals that antagonistic interactions between Pi and Fe availability determine root cell-specific callose deposition to regulate symplastic signaling in the SCN and RAM activity.

Localized Callose Deposition Adjusts RAM Activity to External Pi Status

The epistatically interacting *lpr1lpr2* and *pdr2* mutations cause insensitive and hypersensitive root growth responses to –Pi, respectively. Loss of *PDR2* leads to stem cell differentiation and frequent cell death in the SCN of Pi-deprived roots, phenotypes that are masked in *lpr1lpr2pdr2* plants (Ticconi et al., 2009; Figure S3B). Because stem cell maintenance depends on cell-to-cell communication in the SCN (Gallagher et al., 2014; Perilli et al., 2012; van den Berg et al., 1997), we monitored callose formation in the RAM and observed conditional deposition strictly dependent on Pi status and genotype (Figure 3). In the wild-type on –Pi, callose deposition rapidly inhibits (<12 hr) SHR movement into the QC and developing endodermis. Formation of a middle cortex, as reported for heterozygous *shr* mutants (Koizumi et al., 2012), is consistent with impaired SHR trafficking (Figure 4). Loss of stem cell maintenance and RAM activity are likely consequences. Cell-specific callose accumulation in –Pi is augmented in *pdr2* but is not evident in *lpr1lpr2* or the triple mutant. Therefore, Pi-conditional callose deposition depends on LPR1 function, which is supported by the spatially coincident *pLPR1::GUS* expression domain, and by ectopic callose formation in Pi-starved *p35S::LPR1* roots (Figures 5A–5D).

We previously reported loss of SHR∼GFP fluorescence in the endodermal layer of *pdr2* root meristems on –Pi (Ticconi et al., 2009). Our initial interpretation of unrestricted SHR∼GFP movement beyond the endodermis in *pdr2* was deduced from the observation that endodermal GFP∼SCR expression in *pdr2* also declined on –Pi but was rescued by increasing *SCR* gene dosage. Because *SCR* expression above the basal level depends on SHR activity in the endodermis (Cui et al., 2007), our previous data are consistent with this study, which, however, indicates impaired SHR movement into the endodermis in –Pi.

Previous work has demonstrated the importance of callose deposition and symplastic trafficking in the control of root development (Benitez-Alfonso et al., 2009, 2013; Vatén et al., 2011). Dynamic callose turnover is accomplished by the coordinated action of callose synthases (CALS) and β-1,3-glucanases. Gain-of-function mutations of RAM-expressed *CALS3* lead to uncontrolled callose deposition at the PD during early root development, impaired SHR movement, and a truncated root system (Vatén et al., 2011). Transcript levels of the 12 *CALS* genes in *Arabidopsis* do not respond to Pi status, and none of the viable knockout lines revealed a Pi-dependent root phenotype (data not shown), suggesting redundant and posttranscriptional regulation of callose biosynthesis, as proposed recently (Vatén et al., 2011). Several studies point to a role of ROS-dependent callose deposition for regulating symplastic trafficking (Benitez-Alfonso et al., 2011; Stonebloom et al., 2009). Identification of the thioredoxin GAT1 (GFP ARRESTED TRAFFICKING1) provided genetic evidence that redox regulation of callose deposition and symplastic permeability is essential for RAM maintenance (Benitez-Alfonso et al., 2009). Similar to *gat1* roots, the *rml1* (*root meristemless1*) mutant, which is defective in antioxidant glutathione synthesis and early root development, shows reduced PD conductivity because of elevated callose and ROS accumulation in root tips (Benitez-Alfonso and Jackson, 2009). Although these studies highlight the significance of redox-regulated callose deposition in the execution of root developmental programs,

(B) Root tip morphology, Fe accumulation (Perls), and callose deposition (aniline blue) of *p35S::LPR1* (line #41) after germination on +Pi or −Pi (5 days). Scale bar, 100 μm.
(C) *p35S::SP^{LPR1}∼GFP∼LPR1* expression in a primary root tip. Scale bar, 100 μm.
(D) Fe accumulation (Perls), callose deposition (aniline blue), and ROS formation (C-H2DCFDA and NBT) in *p35S::SP^{LPR1}∼GFP∼LPR1* root tips after transfer of 4-day-old plants to +Pi or −Pi (3 days). Asterisks mark NBT staining that is different from the +Pi condition or the wild-type. Scale bars, 100 μm.
(E) 3D structure of Fet3p (left) and homology model of LPR1 with its predicted trinuclear (T2/T3) Cu cluster (right).
(F) Putative T1 Cu and Fe^{2+} binding sites of LPR1. The experimentally determined residues of Fet3p (green) and predicted residues of LPR1 (blue) are superimposed. Metal ions are shown as spheres. The black dotted lines trace predicted electron transfers from Fe^{2+} to the T1 Cu site. The red dotted line indicates the major contribution of D283 to Fe^{2+} binding of Fet3p (Stoj et al., 2006).
(G) Ferroxidase activity of GFP∼LPR1. Top: specific ferroxidase activity of total protein extracts of transfected tobacco leaves (GFP∼LPR1 or GFP). Shown are the means of four independent transfection experiments (±SE). Bottom: immunoblot analysis of leaf extracts with anti-LPR1 or anti-GFP antibodies.
(H) Cell wall localization of GFP∼LPR1 in *p35S::SP^{LPR1}∼GFP∼LPR1* plants. GFP and PI fluorescence of primary root cells (top row) and of the cell plate during cytokinesis (center row). Also shown is the fluorescence of GFP and FM4-64 (a lipophilic dye decorating endomembranes) after plasmolysis with 150 mM NaCl (bottom row). Scale bars, 10 μm.
(I) Cell wall co-localization of GFP∼LPR1 and PI in *pUBQ10::SP^{LPR1}∼GFP∼LPR1* roots (line #2). Because of the low GFP expression, laser intensity was set to a level inducing autofluorescence in untransformed wild-type (Col) controls. Under these conditions, all *pUBQ10::SP^{LPR1}∼GFP∼LPR1* lines tested, but not the control seedlings (Figure S5C), showed a distinct GFP signal in cell walls (red arrow). Scale bar, 20 μm.
(J) Detection of LPR by immunoblot analysis in cell wall fractions of suspension-cultured *A. thaliana* (Col) cells. Cell wall fractions of intact cells (7 days old) were prepared and lyophilized. LPR1 was reproducibly detected in whole cells and only in the DTT fraction after sequential cell wall extraction. One representative of three independent experiments is shown.
See also Figures S4 and S5.

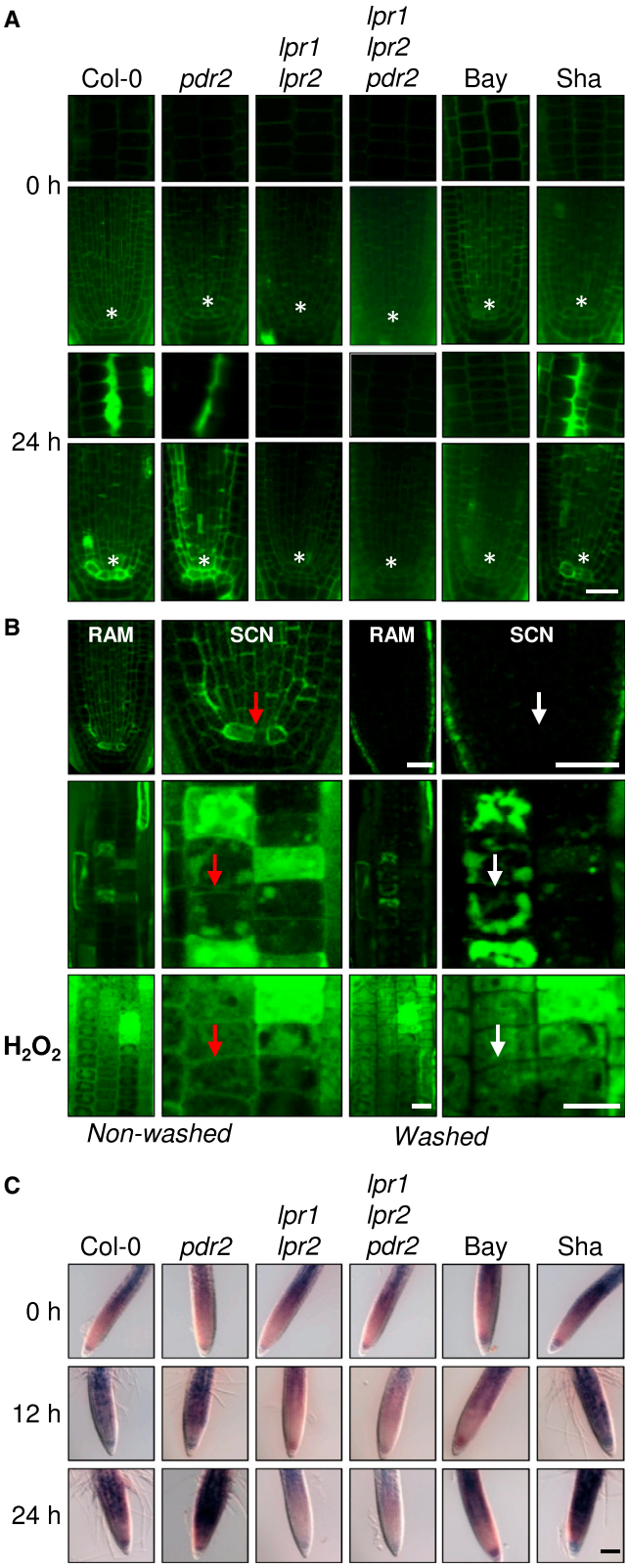

Figure 6. LPR1-Dependent Apoplastic ROS Formation in Low Pi

Shown are the Pi-dependent dynamics of ROS production and distribution in primary root tips.

(A) Carboxy-H2DCFDH staining of ROS in root tips upon transfer of 4-day-old seedlings from +Pi to −Pi medium. Top: cortex cells in the transition zone. Bottom: RAM. Asterisks mark the QC. Scale bar, 50 μm.

(B) Carboxy-H2DCFDA detects apoplastic ROS. Seedlings were imaged immediately after staining for 10 min (non-washed) or after additional washing for stain removal (washed). Top row: RAM and SCN after seedling transfer to −Pi (24 hr). Center row: overview (left) and detail (right) of some stressed cells (showing intracellular staining) in the distal RAM on +Pi. Bottom row: pre-treatment with 10 mM H_2O_2 (15 min) to elevate intracellular and apoplastic ROS. Red and white arrows point to the same cell wall before and after washing, respectively. The data indicate that the dye reports ROS production in the apoplast. Scale bars, 50 μm (top) and 10 μm (bottom).

(C) NBT staining of superoxide in root tips upon transfer to +Pi or −Pi medium. Scale bar, 100 μm.

our work points to a role of Fe-dependent ROS signaling for adjusting callose formation during the perception of an external cue.

LPR1-Dependent Fe Accumulation Controls Callose Deposition in Low Pi

Root Pi sensing depends on LPR1 and external Fe availability. Irrespective of the genotype, Fe absence in –Pi prevents root growth inhibition (Figure 1), as reported for the Col wild-type (Svistoonoff et al., 2007; Ward et al., 2008), and callose deposition (Figure S3C). In the presence of Fe, the contrasting growth responses of *lpr1lpr2* and *pdr2*, as well as their epistatic interaction, correlate strikingly with low and high Fe accumulation in root tips, respectively. The major site of differential Fe accumulation between genotypes is the apoplast of cells within the domain of LPR1-dependent callose deposition, particularly the cell walls of the SCN and elongating cortex cells (Figure 1). Because the mature root zone of all genotypes tested accumulates Fe in –Pi (Figure 1C; Figure S1A), and because long-distance translocation of Fe into the RAM is unlikely (Figure 7D), *LPR1* expression in the root apex and its natural variation determine the growth response to Pi availability (Reymond et al., 2006; Svistoonoff et al., 2007).

We present evidence that the LPR1 MCO functions as a cell-wall-localized ferroxidase (Figure 5; Figure S4). Its close paralog LPR2, which plays a minor but additive role in the response to Pi availability (Svistoonoff et al., 2007), also displays ferroxidase activity (data not shown). Yeast and algal ferroxidases facilitate cellular Fe uptake by providing Fe^{3+} to physically interacting Fe^{3+}-specific permeases (e.g., Ftr1p), whereas related insect and mammalian MCOs mediate cellular Fe efflux in concert with Fe^{2+}-specific permeases (e.g., ferroportin). The exported and subsequently oxidized Fe is loaded onto transferrin for transport, storage, or oxidative stress regulation (Hentze et al., 2004; Lang et al., 2012). However, plant ferroxidases and their roles for Fe homeostasis remain to be explored (Kobayashi and Nishizawa, 2012). Unlike Fet3p in yeast, LPR1 lacks a transmembrane domain, and there is no obvious Ftr1p ortholog in plants. Our data indicate that LPR1 is responsible for apoplastic Fe^{3+} deposition in the interior cell layers of Pi-deprived root tips (Figure 1; Figure S1). Therefore, possible sources of the LPR1 substrate are Fe^{2+}-effluxed by ferroportin (FPN)) or the product of ferric-chelate reductase oxidase (FRO) activities, which reduce apoplast-diffusible Fe^{3+} chelates for IRT1-dependent Fe^{2+} uptake (Kobayashi and Nishizawa, 2012). Although FRO3

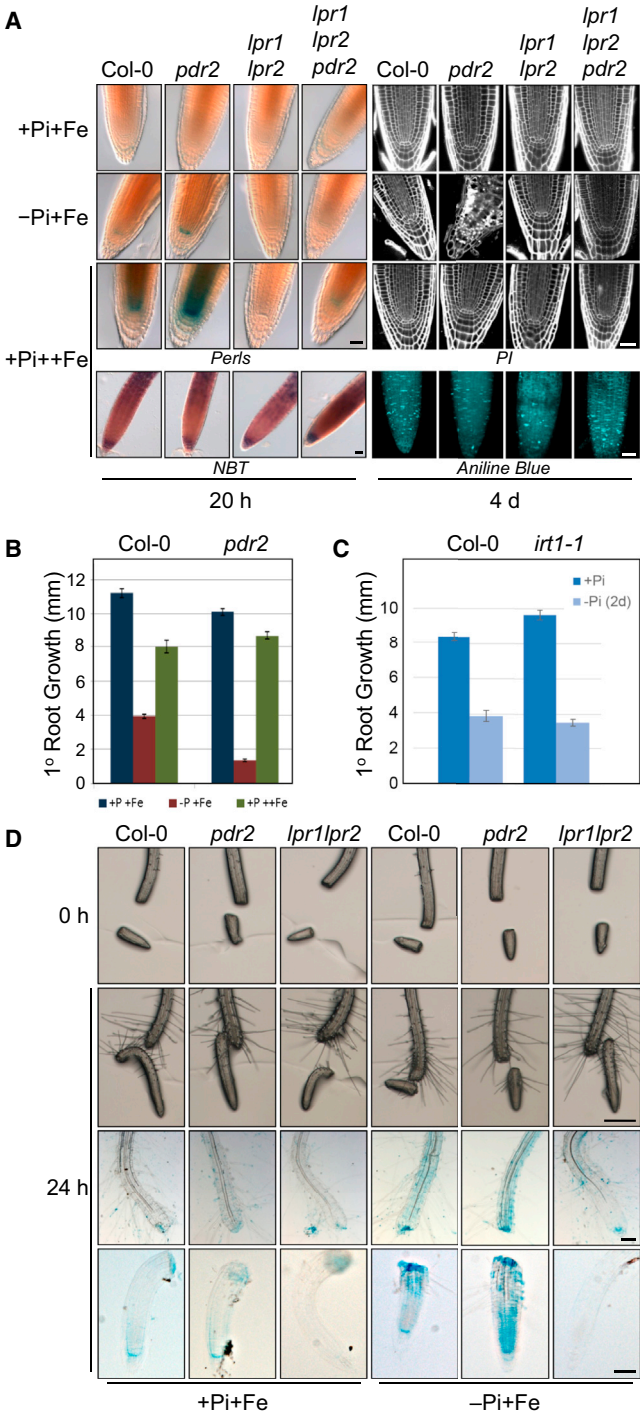

Figure 7. Pi-Fe Antagonism and Local Fe Uptake Adjust RAM Activity to Pi Availability

(A) Comparison of primary root phenotypes after transfer of 4-day-old plants to +Pi+Fe (49.16 μM Fe^{3+}-EDTA), −Pi+Fe (49.24 μM Fe^{3+}-EDTA), or +Pi++Fe (495.1 μM Fe^{3+}-EDTA) medium. Brackets give calculated Fe bioavailabilities. Shown is staining for Fe (Perls), RAM organization (PI), superoxide (NBT), and callose (aniline blue). Scale bars, 50 μm.

(B) Primary root growth after transfer (2 days) to the indicated media (±SE, n = 32–44).

(C) Primary root growth of Col-0 and *irt1-1* seedlings after transfer (2 days) to +Pi or −Pi medium (±SE, n = 12–18).

(D) Plants (4 days) were transferred to +Pi or −Pi medium, and the primary root tips were cut off at the proximal meristem boundary. After 24 hr, the detached root tips were imaged on the same plate (top rows; scale bar, 500 μm) and stained (Perls) for Fe (bottom rows; scale bars, 100 μm).

See also Figure S6.

is expressed in the RAM (Mukherjee et al., 2006), IRT1expression is largely excluded from the root apex (Vert et al., 2002), suggesting only a minor role of IRT1 for Fe^{2+} uptake by root tips (Figure 7C). Whatever the origin of Fe^{2+}, we hypothesize that LPR1-dependent Fe^{3+} production in the apoplast initiates Fe redox cycling as a potential source of ROS (Kosman, 2010; Meguro et al., 2007). Effluxed ascorbate may reduce the LPR1 product to redox-active Fe^{2+} (Grillet et al., 2014), thereby triggering callose deposition and root cell differentiation. Indeed, LPR1 overexpression causes ectopic Fe^{3+} and ROS generation in –Pi (Figure 5D), and genotype-dependent ROS formation in the apoplast is detectable in Pi-deprived root tips (Figure 6). Interestingly, this scenario is reminiscent of the role for Fe in plant defense. Pathogen attack elicits targeted redistribution of Fe^{3+} to the apoplast, where it mediates ROS production, leading to activation of defense genes and localized callose deposition (Aznar et al., 2014; Liu et al., 2007). Fe accumulation and its consequences are also associated with neurodegenerative diseases. During Alzheimer's pathologies, deposits of the redox active amyloid β peptide (Aβ), which binds with high affinities to Fe^{3+} and Cu^{2+}, proficiently generate ROS, causing pervasive oxidative damage. Fenton-type reactions and redox cycling are initiated by Aβ-catalyzed reduction of the bound transition metals (Smith et al., 2007).

The redox activity of LPR1-derived Fe^{3+} is likely controlled by apoplast chemistry (e.g., pH) and the properties of available Fe ligands, including apoplastic Pi. Because of their metal-chelating activity, phosphates are synergistic antioxidants and, therefore, used as food additives (see Codex Alimentarius). Elemental imaging revealed apoplastic co-localization of Pi and Fe in the SCN of Pi-sufficient roots. However, only Fe ions were detectable after transfer to –Pi, suggesting cellular Pi uptake and redox activation of apoplastic Fe (Figure 2). Antagonistic control of Fe redox activity by Pi availability was indicated by exposing roots to 10-fold Fe excess in +Pi. Although Fe hyperaccumulated in root tips in a LPR1-dependent fashion, ROS and callose formation were suppressed, and RAM organization was maintained (Figure 7A). Therefore, dependent on external Pi, the dynamics of apoplastic Fe chelation and speciation likely determine ROS and callose production in the RAM.

It has been proposed that root growth inhibition in –Pi results from general Fe toxicity because of increased Fe bioavailability (Ward et al., 2008). We show that the Fe-mediated growth response to external Pi is under genetic control by *LPR1* and *PDR2*. LPR1-dependent Fe redox cycling and ROS production likely serve as a signal to report apoplastic Pi:Fe ratios and to regulate callose production in the *LPR1* expression domain. Cell-specific callose deposition fine-tunes symplastic communication in the RAM to adjust its activity. *LPR1* and *PDR2* expression is not responsive to Pi status, and LPR1 activity seems to be controlled by substrate availability in the apoplast. *PDR2* encodes the orphan single P5-type ATPase in *Arabidopsis*, AtP5A/MIA (Jakobsen et al., 2005; Ticconi et al., 2009). Loss of

P5A-ATPase activity in yeast leads to pleiotropic phenotypes consistent with a failure to maintain basic ER functions, such as protein folding and processing or trafficking of secretory vesicles (Sørensen et al., 2015). Although general secretion is not severely impaired in *pdr2* root meristems (Ticconi et al., 2004), disruption of *AtP5A/MIA/PDR2* selectively sensitizes a subset of ER quality control responses (Ticconi et al., 2009). Based on the *lpr1lpr2pdr2* mutant phenotype, PDR2 likely restricts LPR output. PDR2 may inhibit secretion of LPR or its associated ferroxidase activity. Likewise, PDR2 may remove oxidized Fe, the product of the LPR reaction. We are currently investigating the mechanism for how AtP5A/MIA/PDR2 controls LPR function.

Callose turnover at cell walls is a widely used strategy to regulate numerous processes in plant development, defense, and stress response, many of which target PD function to adjust intercellular signaling and resource sharing (Burch-Smith and Zambryski, 2012; Zavaliev et al., 2011). ROS signaling initiated by diverse processes is an emerging theme for adjusting PD connectivity (Benitez-Alfonso et al., 2011). Our work highlights the importance of callose-regulated symplastic communication in root meristems for the perception of an abiotic parameter, Pi availability, which likely depends on Fe redox cycling.

EXPERIMENTAL PROCEDURES

Plant Lines and Growth Conditions

A. thaliana accessions Columbia (Col-0), Shahdara (Sha), and Bayreuth (Bay-0) and the Col lines *pdr2*, *lpr1lpr2*, *lpr1lpr2pdr2*, *irt1* (SALK_024525), *pSUC2::GFP*, and *pSHR::SHR-GFP* have been described previously (Imlau et al., 1999; Svistoonoff et al., 2007; Ticconi et al., 2009) or were obtained from the European *Arabidopsis* Stock Center (NASC). GATEWAY technology (Invitrogen) and *Agrobacterium*-mediated transformation were used to generate transgenic lines. Seeds were germinated on 1% (w/v) phyto-agar (Duchefa) using the described salt media. If not stated otherwise, +Pi+Fe medium (referred to as +Pi or high Pi) contained 2.5 mM KH_2PO_4 (pH 5.6), and 50 μM Fe^{3+}-EDTA, whereas –Pi+Fe medium (referred to as –Pi or low Pi) did not contain KH_2PO_4. Both supplements were omitted for the –Pi–Fe condition. The agar was routinely purified and contributed 8–10 μM P and 3–6 μM Fe to the growth medium (Ticconi et al., 2009). Bioavailable Fe^{3+} and Pi were calculated as described previously (Ward et al., 2008). Details on transgenic lines are described in the Supplemental Experimental Procedures.

Statistical Analysis of Root Meristem Size and Cell Elongation

Measurements of elongating epidermal and meristematic root cells were performed after transfer of 4-day-old seedlings to the indicated media. PI-stained roots were imaged by confocal laser-scanning microscopy, 3D projections were generated, and anatomical parameters were calculated as described previously (Berger et al., 1998). Root meristem size was determined as the number of cells in a single trichoblast cell file, starting from the QC to the first elongating cell. The average number of elongating cells in the same cell file was calculated from the first elongating to the first differentiating cell, as determined by the appearance of a root hair bulge. The length of the latter cell type was recorded for calculating the average cell length of differentiating cells. All claims of statistical significance are based on a two-tailed Student's t test.

Histochemical Fe Staining

The Fe-specific Perls staining was adapted from Roschzttardtz et al. (2009). Plants were incubated for up to 30 min in 4% (v/v) HCl, 4% (w/w) K-ferrocyanide (Perls stain), or K-ferricyanide (Turnbull stain). For DAB intensification, plants were washed (dH_2O) and incubated (1 hr) in methanol containing 10 mM Na-azide and 0.3% (v/v) H_2O_2. After washing with 100 mM Na-phosphate buffer (pH 7.4), plants were incubated for up to 30 min in the same buffer containing 0.025% (w/v) DAB (Sigma-Aldrich) and 0.005% (v/v) H_2O_2 but no $CoCl_2$. The reaction was stopped by washing (dH_2O) and optically clearing with chloral hydrate (1 g/ml, 15% glycerol). For preparation of semi-thin (1-μm) sections, roots were fixed as for electron microscopy, but the uranyl-acetate step was omitted. Perls/DAB-stained roots and sections were analyzed on a Zeiss AxioImager.

Electron Microscopy and NanoSIMS Chemical Imaging

Ultra-thin root sections (90 nm) were processed and imaged on a Zeiss Libra 120 transmission electron microscope, and a CAMECA NanoSIMS 50 was used for high-resolution elemental mapping of semi-thin (1-μm) sections as described in the Supplemental Experimental Procedures.

Confocal Laser-Scanning Microscopy and Staining Procedures

Confocal microscopy was done on a Zeiss LSM710. For PI or FM4-64 staining, seedlings were directly imaged in 10 μM PI or 50 μM Synapto Red C2 (Sigma-Aldrich). Callose was stained for 1.5 hr with 0.1% (w/v) aniline blue (AppliChem) in 100 mM Na-phosphate buffer (pH 7.2). Co-localization of GFP and PI was monitored in sequential mode. GUS staining and ROS detection are described in the Supplemental Experimental Procedures.

Statistical Analysis of SHR-GFP Movement

Plants were grown for 4 days on +Pi+Fe agar and transferred to +Pi+Fe or –Pi+Fe medium for the indicated times. Three independent experiments were performed for statistical analysis of SHR-GFP movement into the QC. Plants were counterstained with PI and imaged by confocal laser-scanning microscopy in sequential mode and with identical settings. For statistical analysis, QC cells were identified, and GFP intensity was measured on ImageJ software by setting a region of interest (ROI) to the nucleus. For statistical analysis of the QC-to-stele ratio, the same ROI was subsequently moved into the middle of the stele, and GFP fluorescence was measured again (Koizumi et al., 2012). The QC-to-stele ratio was calculated for each measurement using Microsoft Excel.

Structural Modeling

The predicted 3D structure models of LPR1 (F4I4K5) and LPR2 (Q949X9), encoded by At1g23010 and At1g71040, respectively, were generated using the protein threading method provided by the Protein Homology/AnalogY Recognition Engine, version 2.0 (Phyre2) (Kelley and Sternberg, 2009) with 100% confidence. LPR1 and LPR2 have 78.4% sequence identity and are structurally similar, as indicated by structure superimposition (Zhang and Skolnick, 2005). Final 3D models of LPR1 and LPR2 were submitted to the 3DLigandSite server (Wass et al., 2010) for in silico metal binding prediction, which identified the trinuclear copper cluster (T2/T3) in both proteins. Manual analysis predicted the mononuclear copper binding site (T1) as well as the putative triad of Fe^{2+}-binding amino acid residues in LPR1 and LPR2. These are similar to yeast Fet3p (Stoj et al., 2006) based on multiple sequence alignment (Katoh et al., 2002) of LPR1, LPR2, Fet3p (P38993), and Fet5p (P43561), and on superimposition with the experimental structure of Fet3p. PyMOL (http://www.pymol.org) was used for analysis and generation of figures.

Ferroxidase Assay

Ferroxidase activity was determined using $Fe(NH_4)_2(SO_4)_2 \cdot 6H_2O$ as the electron donor (substrate) and 3-(2-pyridyl)-5,6-bis(2-[5-furylsulfonic acid])-1,2,4-triazine (ferrozine) as a specific Fe^{2+} chelator to scavenge the remaining substrate after the reactions (Erel, 1998). Reactions were carried out in tubes containing 1050 μl buffer (450 mM Na-acetate [pH 5.8], 100 μM $CuSO_4$), 15 μl total protein extract prepared from roots, or 15 μl ceruloplasmin (2.17 μg/ml) as control. After starting the reaction with 225 μl substrate (357 μM) containing 100 μM $CuSO_4$, aliquots (200 μl) were removed at appropriate intervals and transferred to microtiter plate wells for reaction-quenching with 14 μl 18 mM ferrozine. The rate of Fe^{2+} oxidation was calculated from the decreased absorbance at 560 nm using a molar absorptivity of $\varepsilon_{560} = 25{,}400\ M^{-1}\ cm^{-1}$ for the Fe^{2+}-ferrozine complex (Hoopes and Dean, 2004). All reagents except human ceruloplasmin (Athens Research) were purchased from Sigma-Aldrich.

LPR1 Expression Analysis

RNA and cDNA preparation, qRT-PCR, protein extraction, and immunoblot analysis of LPR1 expression are described in the Supplemental Experimental Procedures.

SUPPLEMENTAL INFORMATION

Supplemental Information includes Supplemental Experimental Procedures and six figures and can be found with this article online at http://dx.doi.org/10.1016/j.devcel.2015.02.007.

AUTHOR CONTRIBUTIONS

J.M. designed and performed most experiments and co-wrote the paper. T.T. generated and characterized the *LPR1* transgenic lines. M.H. analyzed LPR1 activity. J.T. assisted J.M. with early experiments. K.L.M. conducted the NanoSIMS experiments. G.H. supervised and performed electron microscopy. D.C.D. modeled LPR structures. K.B. supported and advised on early experiments. S.A. conceived the study, designed experiments, and wrote the manuscript. All authors read, approved, and contributed to the manuscript.

ACKNOWLEDGMENTS

We thank D. Jackson and B. Scheres for seeds; C. Gutjahr, T. Desnos, and C. Wasternack for discussions; the anonymous referees for helpful suggestions; and the Leibniz Association for institutional core funding.

Received: June 12, 2014
Revised: December 12, 2014
Accepted: February 9, 2015
Published: April 20, 2015

REFERENCES

Abel, S. (2011). Phosphate sensing in root development. Curr. Opin. Plant Biol. *14*, 303–309.

Aznar, A., Chen, N.W., Rigault, M., Riache, N., Joseph, D., Desmaële, D., Mouille, G., Boutet, S., Soubigou-Taconnat, L., Renou, J.P., et al. (2014). Scavenging iron: a novel mechanism of plant immunity activation by microbial siderophores. Plant Physiol. *164*, 2167–2183.

Baum, S.F., Dubrovsky, J.G., and Rost, T.L. (2002). Apical organization and maturation of the cortex and vascular cylinder in Arabidopsis thaliana (Brassicaceae) roots. Am. J. Bot. *89*, 908–920.

Beemster, G.T., and Baskin, T.I. (1998). Analysis of cell division and elongation underlying the developmental acceleration of root growth in Arabidopsis thaliana. Plant Physiol. *116*, 1515–1526.

Benitez-Alfonso, Y., and Jackson, D. (2009). Redox homeostasis regulates plasmodesmal communication in Arabidopsis meristems. Plant Signal. Behav. *4*, 655–659.

Benitez-Alfonso, Y., Cilia, M., San Roman, A., Thomas, C., Maule, A., Hearn, S., and Jackson, D. (2009). Control of Arabidopsis meristem development by thioredoxin-dependent regulation of intercellular transport. Proc. Natl. Acad. Sci. USA *106*, 3615–3620.

Benitez-Alfonso, Y., Jackson, D., and Maule, A. (2011). Redox regulation of intercellular transport. Protoplasma *248*, 131–140.

Benitez-Alfonso, Y., Faulkner, C., Pendle, A., Miyashima, S., Helariutta, Y., and Maule, A. (2013). Symplastic intercellular connectivity regulates lateral root patterning. Dev. Cell *26*, 136–147.

Berger, F., Hung, C.Y., Dolan, L., and Schiefelbein, J. (1998). Control of cell division in the root epidermis of Arabidopsis thaliana. Dev. Biol. *194*, 235–245.

Burch-Smith, T.M., and Zambryski, P.C. (2012). Plasmodesmata paradigm shift: regulation from without versus within. Annu. Rev. Plant Biol. *63*, 239–260.

Contento, A.L., and Bassham, D.C. (2012). Structure and function of endosomes in plant cells. J. Cell Sci. *125*, 3511–3518.

Cui, H., Levesque, M.P., Vernoux, T., Jung, J.W., Paquette, A.J., Gallagher, K.L., Wang, J.Y., Blilou, I., Scheres, B., and Benfey, P.N. (2007). An evolutionarily conserved mechanism delimiting SHR movement defines a single layer of endodermis in plants. Science *316*, 421–425.

Dolan, L., Janmaat, K., Willemsen, V., Linstead, P., Poethig, S., Roberts, K., and Scheres, B. (1993). Cellular organisation of the Arabidopsis thaliana root. Development *119*, 71–84.

Erel, O. (1998). Automated measurement of serum ferroxidase activity. Clin. Chem. *44*, 2313–2319.

Gallagher, K.L., Sozzani, R., and Lee, C.M. (2014). Intercellular protein movement: deciphering the language of development. Annu. Rev. Cell Dev. Biol. *30*, 207–233.

Grillet, L., Ouerdane, L., Flis, P., Hoang, M.T., Isaure, M.P., Lobinski, R., Curie, C., and Mari, S. (2014). Ascorbate efflux as a new strategy for iron reduction and transport in plants. J. Biol. Chem. *289*, 2515–2525.

Helariutta, Y., Fukaki, H., Wysocka-Diller, J., Nakajima, K., Jung, J., Sena, G., Hauser, M.T., and Benfey, P.N. (2000). The SHORT-ROOT gene controls radial patterning of the Arabidopsis root through radial signaling. Cell *101*, 555–567.

Hentze, M.W., Muckenthaler, M.U., and Andrews, N.C. (2004). Balancing acts: molecular control of mammalian iron metabolism. Cell *117*, 285–297.

Hoegger, P.J., Kilaru, S., James, T.Y., Thacker, J.R., and Kües, U. (2006). Phylogenetic comparison and classification of laccase and related multicopper oxidase protein sequences. FEBS J. *273*, 2308–2326.

Hoopes, J.T., and Dean, J.F. (2004). Ferroxidase activity in a laccase-like multicopper oxidase from Liriodendron tulipifera. Plant Physiol. Biochem. *42*, 27–33.

Imlau, A., Truernit, E., and Sauer, N. (1999). Cell-to-cell and long-distance trafficking of the green fluorescent protein in the phloem and symplastic unloading of the protein into sink tissues. Plant Cell *11*, 309–322.

Jakobsen, M.K., Poulsen, L.R., Schulz, A., Fleurat-Lessard, P., Møller, A., Husted, S., Schiøtt, M., Amtmann, A., and Palmgren, M.G. (2005). Pollen development and fertilization in Arabidopsis is dependent on the MALE GAMETOGENESIS IMPAIRED ANTHERS gene encoding a type V P-type ATPase. Genes Dev. *19*, 2757–2769.

Katoh, K., Misawa, K., Kuma, K., and Miyata, T. (2002). MAFFT: a novel method for rapid multiple sequence alignment based on fast Fourier transform. Nucleic Acids Res. *30*, 3059–3066.

Kellermeier, F., Armengaud, P., Seditas, T.J., Danku, J., Salt, D.E., and Amtmann, A. (2014). Analysis of the root system architecture of Arabidopsis provides a quantitative readout of crosstalk between nutritional signals. Plant Cell *26*, 1480–1496.

Kelley, L.A., and Sternberg, M.J. (2009). Protein structure prediction on the Web: a case study using the Phyre server. Nat. Protoc. *4*, 363–371.

Kobayashi, T., and Nishizawa, N.K. (2012). Iron uptake, translocation, and regulation in higher plants. Annu. Rev. Plant Biol. *63*, 131–152.

Koizumi, K., Hayashi, T., Wu, S., and Gallagher, K.L. (2012). The SHORT-ROOT protein acts as a mobile, dose-dependent signal in patterning the ground tissue. Proc. Natl. Acad. Sci. USA *109*, 13010–13015.

Kosman, D.J. (2010). Redox cycling in iron uptake, efflux, and trafficking. J. Biol. Chem. *285*, 26729–26735.

Lang, M., Braun, C.L., Kanost, M.R., and Gorman, M.J. (2012). Multicopper oxidase-1 is a ferroxidase essential for iron homeostasis in Drosophila melanogaster. Proc. Natl. Acad. Sci. USA *109*, 13337–13342.

Liu, G., Greenshields, D.L., Sammynaiken, R., Hirji, R.N., Selvaraj, G., and Wei, Y. (2007). Targeted alterations in iron homeostasis underlie plant defense responses. J. Cell Sci. *120*, 596–605.

Meguro, R., Asano, Y., Odagiri, S., Li, C., Iwatsuki, H., and Shoumura, K. (2007). Nonheme-iron histochemistry for light and electron microscopy: a historical, theoretical and technical review. Arch. Histol. Cytol. *70*, 1–19.

Moore, K.L., Schröder, M., Wu, Z., Martin, B.G., Hawes, C.R., McGrath, S.P., Hawkesford, M.J., Feng Ma, J., Zhao, F.J., and Grovenor, C.R. (2011). High-resolution secondary ion mass spectrometry reveals the contrasting subcellular distribution of arsenic and silicon in rice roots. Plant Physiol. *156*, 913–924.

Mukherjee, I., Campbell, N.H., Ash, J.S., and Connolly, E.L. (2006). Expression profiling of the Arabidopsis ferric chelate reductase (FRO) gene family reveals differential regulation by iron and copper. Planta *223*, 1178–1190.

Nakajima, K., Sena, G., Nawy, T., and Benfey, P.N. (2001). Intercellular movement of the putative transcription factor SHR in root patterning. Nature *413*, 307–311.

Paquette, A.J., and Benfey, P.N. (2005). Maturation of the ground tissue of the root is regulated by gibberellin and SCARECROW and requires SHORTROOT. Plant Physiol. *138*, 636–640.

Péret, B., Clément, M., Nussaume, L., and Desnos, T. (2011). Root developmental adaptation to phosphate starvation: better safe than sorry. Trends Plant Sci. *16*, 442–450.

Perilli, S., Di Mambro, R., and Sabatini, S. (2012). Growth and development of the root apical meristem. Curr. Opin. Plant Biol. *15*, 17–23.

Petricka, J.J., Winter, C.M., and Benfey, P.N. (2012). Control of Arabidopsis root development. Annu. Rev. Plant Biol. *63*, 563–590.

Reymond, M., Svistoonoff, S., Loudet, O., Nussaume, L., and Desnos, T. (2006). Identification of QTL controlling root growth response to phosphate starvation in Arabidopsis thaliana. Plant Cell Environ. *29*, 115–125.

Roschzttardtz, H., Conéjéro, G., Curie, C., and Mari, S. (2009). Identification of the endodermal vacuole as the iron storage compartment in the Arabidopsis embryo. Plant Physiol. *151*, 1329–1338.

Sabatini, S., Heidstra, R., Wildwater, M., and Scheres, B. (2003). SCARECROW is involved in positioning the stem cell niche in the Arabidopsis root meristem. Genes Dev. *17*, 354–358.

Sánchez-Calderón, L., López-Bucio, J., Chacón-López, A., Cruz-Ramírez, A., Nieto-Jacobo, F., Dubrovsky, J.G., and Herrera-Estrella, L. (2005). Phosphate starvation induces a determinate developmental program in the roots of *Arabidopsis thaliana*. Plant Cell Physiol. *46*, 174–184.

Scheres, B. (2007). Stem-cell niches: nursery rhymes across kingdoms. Nat. Rev. Mol. Cell Biol. *8*, 345–354.

Smith, D.G., Cappai, R., and Barnham, K.J. (2007). The redox chemistry of the Alzheimer's disease amyloid beta peptide. Biochim. Biophys. Acta *1768*, 1976–1990.

Sørensen, D.M., Holen, H.W., Holemans, T., Vangheluwe, P., and Palmgren, M.G. (2015). Towards defining the substrate of orphan P5A-ATPases. Biochim. Biophys. Acta *1850*, 524–535.

Stoj, C.S., Augustine, A.J., Zeigler, L., Solomon, E.I., and Kosman, D.J. (2006). Structural basis of the ferrous iron specificity of the yeast ferroxidase, Fet3p. Biochemistry *45*, 12741–12749.

Stonebloom, S., Burch-Smith, T., Kim, I., Meinke, D., Mindrinos, M., and Zambryski, P. (2009). Loss of the plant DEAD-box protein ISE1 leads to defective mitochondria and increased cell-to-cell transport via plasmodesmata. Proc. Natl. Acad. Sci. USA *106*, 17229–17234.

Svistoonoff, S., Creff, A., Reymond, M., Sigoillot-Claude, C., Ricaud, L., Blanchet, A., Nussaume, L., and Desnos, T. (2007). Root tip contact with low-phosphate media reprograms plant root architecture. Nat. Genet. *39*, 792–796.

Ticconi, C.A., Delatorre, C.A., Lahner, B., Salt, D.E., and Abel, S. (2004). *Arabidopsis pdr2* reveals a phosphate-sensitive checkpoint in root development. Plant J. *37*, 801–814.

Ticconi, C.A., Lucero, R.D., Sakhonwasee, S., Adamson, A.W., Creff, A., Nussaume, L., Desnos, T., and Abel, S. (2009). ER-resident proteins PDR2 and LPR1 mediate the developmental response of root meristems to phosphate availability. Proc. Natl. Acad. Sci. USA *106*, 14174–14179.

van den Berg, C., Willemsen, V., Hendriks, G., Weisbeek, P., and Scheres, B. (1997). Short-range control of cell differentiation in the Arabidopsis root meristem. Nature *390*, 287–289.

Vatén, A., Dettmer, J., Wu, S., Stierhof, Y.D., Miyashima, S., Yadav, S.R., Roberts, C.J., Campilho, A., Bulone, V., Lichtenberger, R., et al. (2011). Callose biosynthesis regulates symplastic trafficking during root development. Dev. Cell *21*, 1144–1155.

Vert, G., Grotz, N., Dédaldéchamp, F., Gaymard, F., Guerinot, M.L., Briat, J.F., and Curie, C. (2002). IRT1, an Arabidopsis transporter essential for iron uptake from the soil and for plant growth. Plant Cell *14*, 1223–1233.

Ward, J.T., Lahner, B., Yakubova, E., Salt, D.E., and Raghothama, K.G. (2008). The effect of iron on the primary root elongation of Arabidopsis during phosphate deficiency. Plant Physiol. *147*, 1181–1191.

Wass, M.N., Kelley, L.A., and Sternberg, M.J. (2010). 3DLigandSite: predicting ligand-binding sites using similar structures. Nucleic Acids Res. *38*, W469–W473.

Wu, S., Lee, C.M., Hayashi, T., Price, S., Divol, F., Henry, S., Pauluzzi, G., Perin, C., and Gallagher, K.L. (2014). A plausible mechanism, based upon Short-Root movement, for regulating the number of cortex cell layers in roots. Proc. Natl. Acad. Sci. USA *111*, 16184–16189.

Zavaliev, R., Ueki, S., Epel, B.L., and Citovsky, V. (2011). Biology of callose (β-1,3-glucan) turnover at plasmodesmata. Protoplasma *248*, 117–130.

Zhang, Y., and Skolnick, J. (2005). TM-align: a protein structure alignment algorithm based on the TM-score. Nucleic Acids Res. *33*, 2302–2309.